European Journal of Nuclear Medicine and Molecular Imaging (2022) 49:2618–2633
https://doi.org/10.1007/s00259-022-05750-8

ORIGINAL ARTICLE

Design, synthesis, and preclinical evaluation of a novel bifunctional macrocyclic chelator for theranostics of cancers

Jianfeng Xu[1,2] · Fei Cai[1,2] · Zhigang Luo[2] · Wenbin Fan[2] · Juan Dai[2] · Jingjing Cui[2] · Shihong Li[2] · Changran Geng[1] · Qihuang Zheng[3] · Zheng Wang[2] · Xiaobin Tang[1]

Received: 27 September 2021 / Accepted: 1 March 2022 / Published online: 26 March 2022

Abstract

Purpose This study was to design and synthesize a novel bifunctional chelator, named Dar, primarily validated by conjugating to tumor targeting motifs, labeled with radiometals, and performed preclinical evaluation of tumor imaging and cancer therapy in murine tumor models.

Method The designed Dar was synthesized and characterized by X-ray crystallography, $^{1}H/^{13}C$ NMR, and mass spectrometry. Dar-PSMA-617 was conjugated and radiolabeled with ^{68}Ga, ^{177}Lu, and ^{89}Zr. The in vivo behavior of $^{68}Ga/^{89}Zr$-labeled Dar-PSMA-617 were evaluated using micro-PET imaging and biodistribution from image quantitation and tissue radioactivity counting, with $^{68}Ga/^{89}Zr$-labeled NOTA/DOTA/DFO-PSMA-617 analogs as controls, respectively. The [^{177}Lu]-Dar-PSMA-617, with [^{177}Lu]-DOTA-PSMA-617 as control, was evaluated in competitive cell uptake, tumor cell internalization, and efflux studies. The treatment efficacy of [^{177}Lu]Lu-Dar-PSMA-617, with [^{177}Lu]Lu-DOTA-PSMA-617 as control, was evaluated in PSMA-positive LNCaP tumor-bearing mice. In addition, the ability of Dar for radiolabeling nanobody was tested by conjugating Dar to KN035 nanobody. The resultant [^{89}Zr]Zr-Dar-KN035 nanobody, with [^{89}Zr]Zr-DFO-KN035 as control, was evaluated by micro-PET imaging and biodistribution in a mouse model bearing MC38&MC38-hPD-L1 colon cancer.

Results ^{68}Ga, ^{89}Zr, and ^{177}Lu-radiolabeled Dar-PSMA-617 complexes were able to be produced under mild condition with high radiochemical yield and purity successfully. [^{177}Lu]Lu-Dar-PSMA-617 had higher cellular uptake yet similar internalization and efflux properties in LNCaP cells, as compared to [^{177}Lu]Lu-DOTA-PSMA-617. Micro-PET images demonstrated significantly higher tumor uptake of [^{68}Ga]Ga-Dar-PSMA-617, than that of the analog [^{68}Ga]Ga-DOTA-PSMA-617. The tumor uptake values of [^{68}Ga]Ga-Dar-PSMA-617 at multiple time points are comparable to that of [^{68}Ga]Ga-NOTA-PSMA-617, although a higher and persistently prolonged kidney retention was resulted in during the study period. The Dar chelator can also successfully mediate the radiolabeling with ^{89}Zr, while the resultant [^{89}Zr]Zr-Dar-PSMA-617 demonstrated a similar biodistribution with [^{89}Zr]Zr-DFO-PSMA-617 measured at 96 h p.i. The treatment with [^{177}Lu]Lu-Dar-PSMA-617 significantly inhibited the tumor growth, showing much better efficacy than that of [^{177}Lu]Lu-DOTA-PSMA-617 at the same injected radioactivity and mass dose. Dar was covalently linked to KN035 nanobody and enabled radiolabeling with ^{89}Zr in high yield and radiochemical purity at room temperature. The resultant [^{89}Zr]Zr-Dar-KN035, with [^{89}Zr]Zr-DFO-KN035 as control, demonstrated superior tumor uptake and detection capability in PET imaging studies.

Conclusion The Dar, as a novel bifunctional chelator for medicating the labeling of radiometals onto tumor targeting carriers, was successfully synthesized and chemically characterized. Test radiolabeling, on PSMA-617 and a nanobody as tool targeting molecule carriers, demonstrated the Dar has potential as a universal bifunctional chelator for radiolabeling various radiometals (at least ^{68}Ga, ^{177}Lu, and ^{89}Zr tested) commonly used for clinical imaging and therapy. Using a novel Dar chelator results in altered in vivo behavior of the carriers even though labeled with the same nuclide. This capability makes Dar an alternative to the existing choices for radiolabeling new carrier molecules with various radiometals, especially the radiometals with large radius.

Keywords Dar · Dar-PSMA-617 · Radiolabeled Dar-PSMA-617 complexes · DOTA-PSMA-617 · Dar-KN035 · Theranostics

This article is part of the Topical Collection on Radiopharmacy.

Extended author information available on the last page of the article

Introduction

In recent years, continuously innovated technologies in nuclear reactors and accelerators have emerged for the production of radionuclides [1, 2]. A variety of radiometal-labeled medicines and drug candidates have been rapidly developed with nuclides such as ^{64}Cu, ^{67}Cu, ^{68}Ga, ^{89}Zr, ^{99m}Tc, ^{177}Lu, ^{188}Re, ^{225}Ac, and ^{227}Th [3, 4]. Since 2016, the FDA has approved eleven radiopharmaceuticals, including five metal radiopharmaceuticals. Additionally, more than two-thirds of radiopharmaceuticals registered in Clinical Trials phase III are the radiometal-labeled drug conjugates. Normally, radiometal needs a bifunctional chelator and proper linker to targeting molecules, such as peptides, antibodies, or small molecules, to achieve specific binding with tumor tissue in vivo [5, 6]. At present, the selection of bifunctional chelator is mainly considered from many aspects such as pharmacokinetics, thermodynamic stability, tumor targeting affinity, and most of time depending on the commercial availability [7–9].

Bifunctional chelating agents can be divided into two categories: chain and cyclic chelators in terms of structure [10, 11]. Chain chelators, including DTPA and DFO, are the most commonly used for radiometal chelation, with DFO as a prominent chelating agent for ^{89}Zr-radiolabeled targeted molecule in PET imaging [12, 13]. In general, macrocyclic analogs are more thermodynamically stable than the acyclic chelating agents, even if their coordinating donors are similar, due to the macrocyclic effect [10, 14, 15]. For example, changing the DFO structure into a ring-shaped chelator improves the stability, such as FSC and TAFC [16–18]. At present, the structural modification is mainly based on the cyclic chelating agent itself [19, 20]. On the other hand, NOTA and DOTA are the two most widely used macrocyclic chelators used for the coordination of ^{68}Ga and ^{177}Lu [21–25]. DOTA derivatives need to be heated over 95 °C to complete radiolabeling with ^{89}Zr, which is not suitable for temperature-sensitive targeting molecules such as antibodies [26, 27]. Current bifunctional chelating agents are only used for similar radioactive metals, and do not have the ability to coordinate radioactive metals with different valence states under mild conditions. Therefore, it is in need to invent a new class of bifunctional chelating agent for multiple types of radiometals to serve rapidly growing radiopharmaceutical application.

Studies back to the late 1990s reported a series of macrocyclic compounds synthesized to mimic the function of biological enzymes [28, 29]. This type of cyclic chelators had been designed to have multiple donors such as phenolic oxygen, pyridine nitrogen, and aliphatic nitrogen to chelate different kinds of metal ions. The resurgence of interest in radionuclide theranostics necessitates a more convenient bifunctional chelator to accommodate various metals. In the present study, we reported a new structure by introducing additional four carboxyl groups into the basic structure of a macrocyclic compound to form a new bifunctional chelating agent, named Dar, (2,2′,2″,2‴-(5^2,13^2-dihydroxy-5^5,13^5-dimethyl-3,7,11,15-tetraaza-1,9(2,6)-dipyridina-5,13(1,3)-dibenzenacyclohexadecaphane-3,7,11,15-tetrayl) tetraacetic acid). This new class of bifunctional macrocyclic chelator is designed to be used to coordinate with a variety of radioactive metal ions through four kinds of coordination donors: phenolic oxygen, carboxyl oxygen, pyridine nitrogen, and aliphatic nitrogen. The newly introduced four carboxyl groups also provide coupling sites for targeting molecules. With PSMA-617 as a tool compound of small molecule/peptide and a nanobody as a tool biologic protein [30, 31], the Dar was conjugated and used to mediate the radiolabeling with ^{68}Ga, ^{89}Zr, or ^{177}Lu. The radiochemistry and the properties of the resultant products were tested both in vitro and in vivo on mouse models with relevant xenografts.

Materials and methods

Materials and instruments

Radionuclide ^{68}Ga was obtained from ^{68}Ge-^{68}Ga generator (Cyclotron Co., Ltd., Russia). ^{89}Zr was obtained from an onsite accelerator (HM-20, Sumitomo Heavy Industries, Ltd., Japan). ^{177}Lu was purchased from Isotopen Technologien München AG (Germany).

Mice-bearing LNCaP xenografts were obtained from Biocytogen (Beijing, China). LNCaP cell line was purchased from ATCC. SD rats and C57BL/6 N mice were obtained from Charles River Laboratories (Zhejiang, China). MC38&MC38-hPD-L1 tumor-bearing mice were constructed from C57BL/6 N mice and provided by Mitro Biotechnology Co., Ltd. (Nanjing, China). All animal studies were performed in accordance with the protocols provided in the Guide for the Care and Use of Medical Laboratory Animals (Ministry of Health, China).

Micro-PET (SNPC-103, Pingseng Healthcare Inc., Kunshan, China) and micro-SPECT (NanoScan, Mediso Medical Imaging Systems, Budapest, Hungary) experiments were performed using pre-clinical imaging scanners for small-animal imaging. A γ-counter (GC-1200) was purchased from Anhui UstcZonkia Scientific Instruments Co., Ltd. X-ray diffraction analysis was performed on a Rigaku Synergy X-ray diffractometer (CuK$_\alpha$ $\lambda = 1.54184$ Å radiation).

Preparation and characterization of Dar

The Dar molecule was synthesized by coupling of compound A [28] with benzyl bromoacetate followed by hydrolysis, as

shown in Fig. 1 and Supplementary Information. The chemical structure of Dar was confirmed and characterized by ^{1}H and ^{13}C NMR spectroscopy and LC–MS analysis (Supplementary Information).

Preparation and crystal structure analysis of Ga-Dar and Lu-Dar complexes

The complexes of Dar with gallium and lutetium were prepared, recrystallized, and analyzed by X-ray diffraction, as described in the Supplementary Information.

Synthesis of Dar-PSMA-617 and Dar-KN035

The structures and synthetic routes of Dar-PSMA-617 and Dar-KN035 are shown in Fig. 1. The detailed preparation and characterization of these two precursors for labeling of radiometals are provided in the Supplementary Information.

Radiolabeling with ^{68}Ga, ^{89}Zr, and ^{177}Lu

Dar-PSMA-617 (0.010 mg) was mixed with [^{68}Ga]$GaCl_3$ or [^{177}Lu]$LuCl_3$ solution (370 MBq) in acetate buffer (pH 4.5) and incubated for 10 min at room temperature, respectively. Dar-PSMA-617 (0.10 mg) was incubated with [^{89}Zr]$ZrCl_4$ (370 MBq) in sodium oxalate buffer solution (pH 7.0) and incubated for 2 h at room temperature. Subsequently, the reaction solution was purified by C18 cartridge to obtain the radiolabeled products. All radiolabeled peptides were analyzed with radio-HPLC. The in vitro stability of ^{68}Ga/^{89}Zr/^{177}Lu-Dar-PSMA-617 was tested with PBS (pH 7.0) and BSA (pH 7.0) at 37 °C. The compounds were analyzed by radio-TLC (AR-2000, Bioscan) at different time points ([^{68}Ga]Ga-Dar-PSMA-617 at 1, 3, 5, and 6 h, [^{89}Zr]Zr-Dar-PSMA-617 at 1, 3, 5, 7, and 9 days, [^{177}Lu]Lu-Dar-PSMA-617 at 1, 3, 6, 9, and 10 days). The partition coefficients of [^{177}Lu]Lu-Dar-PSMA-617 and [^{177}Lu]Lu-DOTA-PSMA-617 were determined in a 50%:50% (v/v) mixture of n-octanol and 25 mM phosphate buffer (pH = 7.4).

To prepare [^{89}Zr]Zr-Dar-KN035, 37 MBq ^{89}Zr oxalate stock solution was added to Dar-KN035 solution (10 mg). The mixture was adjusted to pH 7.0 with 0.1 M Na_2CO_3 solution, and reacted at room temperature for 2 h. The crude product was purified with saline through PD-10 column, and the [^{89}Zr]Zr-Dar-KN035 solution was obtained.

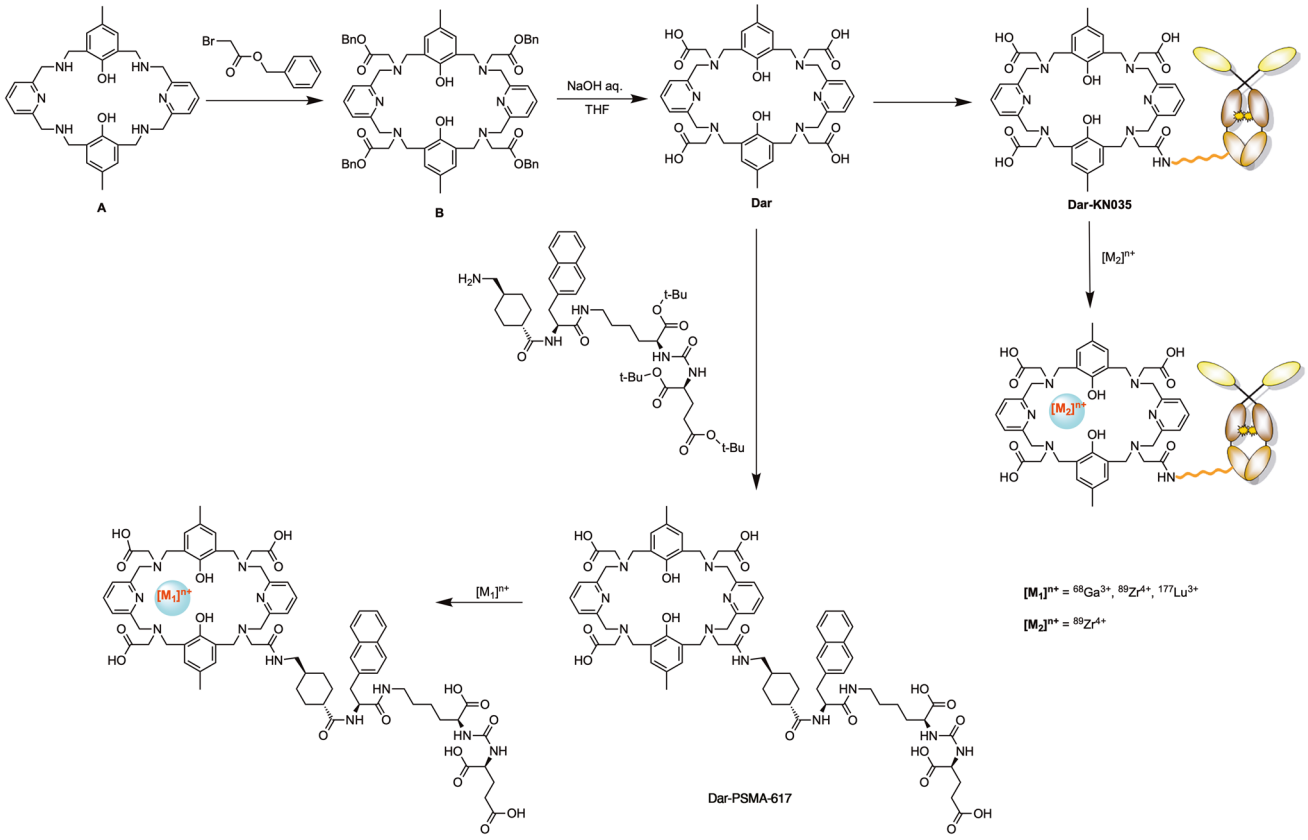

Fig. 1 Synthetic and radiolabeling scheme of Dar-PSMA-617 and Dar-KN035

Micro-PET imaging studies

Micro-PET experiments of radiolabeled Dar-PSMA-617 were conducted using mice-bearing LNCaP xenografts, which were administered intravenously with approximately 3.7 MBq of tracer through the tail vein. MC38&MC38-hPD-L1 bilateral colon cancer model mice were used for micro-PET imaging of radiolabeled Dar-KN035. The mice were positioned in the scanner after anesthetizing with isoflurane and performed whole-body scan at different time points after intravenous injection with tracers, respectively. The scan time points of [^{68}Ga]Ga-Dar-PSMA-617 were 5, 15, 25 min, 2, 3, 4, and 6 h. The scan time points of [^{89}Zr]Zr-Dar-PSMA-617 were 5, 15, 25, 35, 45 min, 1, 4, 24, 48, 72, 96, 168, and 216 h and that of [^{89}Zr]Zr-Dar-KN035 were 4, 24, 72, and 168 h. The time point of the control group corresponds to the experimental group. The mice were scanned for 10–30 min at 350–650 keV of photopeak window. At each time point, CT scans were conducted before/after PET scans. The images were reconstructed and decay-corrected using the PMOD software. The region of interest (ROI) was manually drawn over major organs and tumor. For quantification of radiotracer accumulation in lesions, the target mean-to-background mean ratios were calculated. The results are shown as the percentage of the injected dose per gram (%ID/g). Data are presented as the average ± standard deviation (SD).

Ex vivo biodistribution

LNCaP tumor-bearing mice were injected via the tail vein with 3.7 MBq of [^{89}Zr]Zr-DFO-PSMA-617 and [^{89}Zr]Zr-Dar-PSMA-617 ($n = 3$), and then sacrificed by cervical dislocation at 96-h post injection. LNCaP tumor-bearing mice were injected via the tail vein with 37 MBq of [^{177}Lu]Lu-DOTA-PSMA-617 and [^{177}Lu]Lu-Dar-PSMA-617 ($n = 3$), and then sacrificed by cervical dislocation at 72-h post injection. MC38&MC38-hPD-L1 tumor-bearing mice were injected via the tail vein with 3.7 MBq of [^{89}Zr]Zr-DFO-KN035 and [^{89}Zr]Zr-Dar-KN035 ($n = 3$), and then sacrificed by cervical dislocation at 168-h post injection. Blood was withdrawn from the heart for approximately 0.2–0.5 mL, and the selected organs/tissues of the heart, liver, spleen, lungs, kidneys, pancreas, stomach, small intestine, large intestine, muscle, brain, tibia, arthrosis, and tumor were collected. The collected organs/tissues were weighted and counted using an automated gamma counter (GC-1200, Anhui Ustc Zonkia Scientific Instruments Co., Ltd).

Pharmacokinetics

A total of 2.96 MBq of [^{89}Zr]Zr-Dar and [^{89}Zr]Zr-Dar-PSMA-617 was injected intravenously into male SD rats ($n = 12$) respectively, and 100–200 μL of jugular bulb blood was drawn at 1, 2, 3, 4, 5, 6, 8, 12, 24, 48, 72, 96, 120, 144, and 168 h after intravenous injection. At each time point, 6 males were collected from each group, and 12 animals were cross-collected. Radioactivity for collected blood samples was counted for 30 s by using the γ-counter. The values are expressed as %ID/g.

Cell uptake, internalization, and efflux studies

For cell uptake and internalization studies, 10^6 LNCaP cells were seeded in poly (L-lysine)-coated 24-well cell culture plates at 37 °C in an environment of humidified air containing 5% CO_2 for 24 h. The medium was removed and 250 μL of radiolabeled [^{177}Lu]Lu-Dar-PSMA-617 was replaced for 45 min. One plate was incubated at 37 °C and the second one at 4 °C to inhibit the internalization. The specificity of the ligands was proofed by adding 500 μM of 2-(phosphonomethyl)-pentanedioic acid (2-PMPA, Axxora, Loerrach, Germany). After incubation, the cells were washed three times with 1 mL ice cold PBS. To determine the surface-bound activity, cells were incubated twice with 0.5 mL of glycine–HCl in PBS (50 mM, pH 2.8) each for 5 min at room temperature.

Micro-SPECT imaging studies

[^{177}Lu]Lu-Dar-PSMA-617 and [^{177}Lu]Lu-DOTA-PSMA-617 SPECT scans were performed at 2, 24, 72, and 120 h after i.v. injection (37 MBq per mouse) on LNCaP tumor-bearing mice. At each time point, the mice were positioned in the scanner after anesthetizing with isoflurane and scanned for 10–30 min. CT scans were conducted before/after SPECT scans. The images were reconstructed and decay-corrected using the PMOD software. The tracer uptake quantified as percentage injected dose per gram (%ID/g) in major organs/tissues and tumor was determined by regions of interest (ROI) analyses on the images.

Efficacy studies

LNCaP tumor-bearing mice were used for efficacy evaluation of [^{177}Lu]Lu-Dar-PSMA-617 vs. [^{177}Lu]Lu-DOTA-PSMA-617. The mice were divided into 6 groups (7–10 mice for each group): saline group, 9.25 MBq [^{177}Lu]Lu-Dar-PSMA-617, 18.5 MBq [^{177}Lu]Lu-Dar-PSMA-617, 37 MBq [^{177}Lu]Lu-Dar-PSMA-617, 18.5 MBq [^{177}Lu]Lu-DOTA-PSMA-617, and 37 MBq [^{177}Lu]Lu-DOTA-PSMA-617 groups. Body weights and tumor volumes were measured every day.

Statistical analysis

Quantitative data are expressed as mean ± standard deviation (SD). Mean between different groups were compared using Student's t-test, and $P < 0.05$ indicates statistical significance (*$P < 0.05$, **$P < 0.01$, and ***$P < 0.001$).

Results

Chemistry and radiochemistry

The bifunctional chelator Dar was synthesized and characterized by ^{1}H NMR, ^{13}C NMR, and LC–MS (Supplementary Figs. 1–3). The Dar-PSMA-617 was obtained as a white solid with HPLC purity > 95% and characterized by ^{1}H NMR and LC–MS (Supplementary Figs. 4–5). The Dar-KN035 was obtained as a solution of 1.438 mg/mL in NaOAc buffer (0.1 M, pH 6.5). Dar-PSMA-617 was successfully radiolabeled with ^{68}Ga, ^{89}Zr, and ^{177}Lu at room temperature in high radiochemical purity (> 97%) as determined by radio-HPLC and radio-TLC. [^{68}Ga]Ga-Dar-PSMA-617 was determined by HPLC and its structure was confirmed by LC–MS of [^{Nat}Ga]Ga-Dar-PSMA-617 (Supplementary Figs. 6–9). The radiometal-labeled complexes are stable in normal buffers and serum (Fig. 2). The radiochemical purity of [^{89}Zr]Zr-Dar-KN035 was 96%.

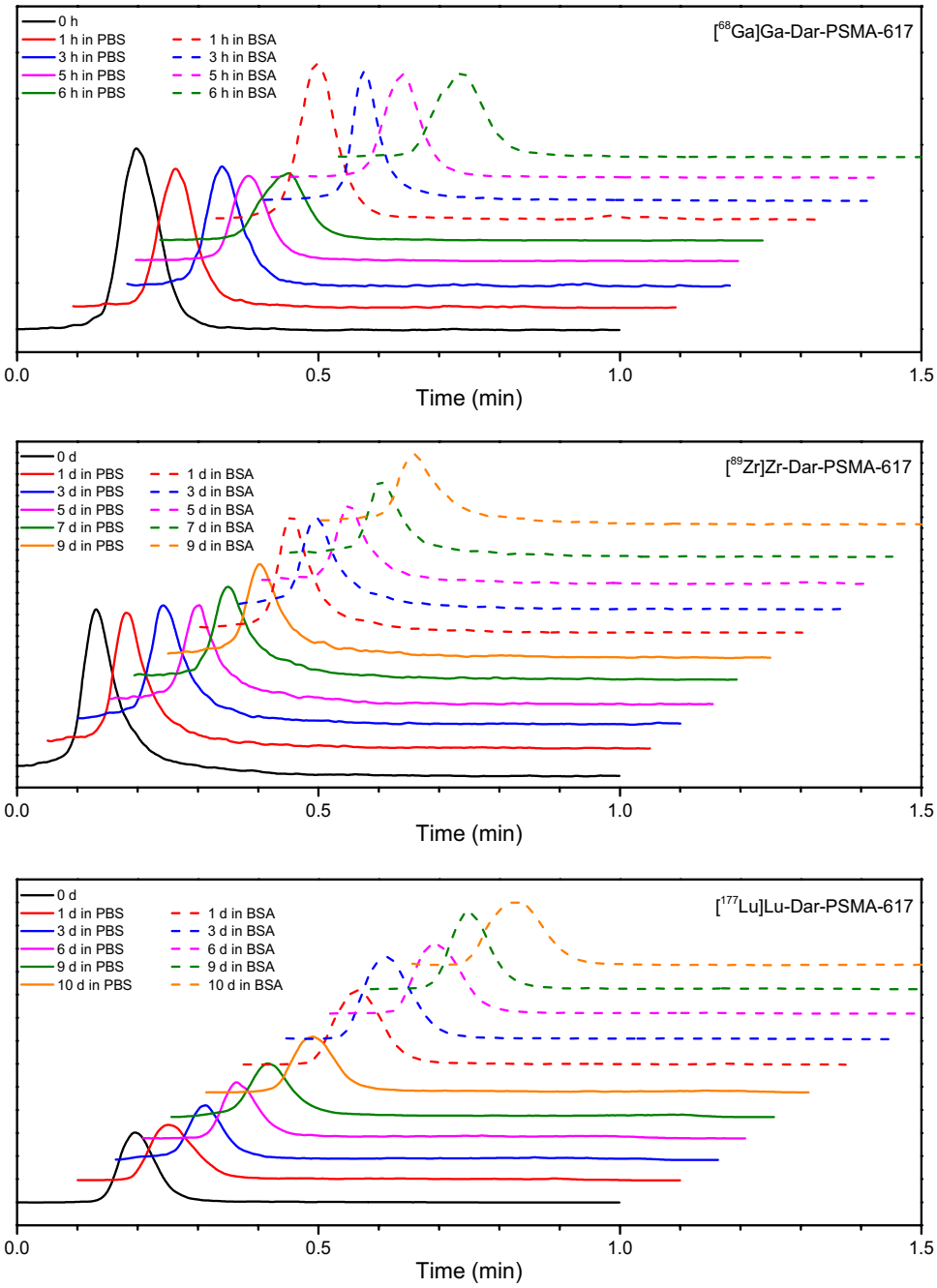

Fig. 2 Radio-TLC chromatogram of [^{68}Ga]Ga-Dar-PSMA-617, [^{89}Zr]Zr-Dar-PSMA-617, and [^{177}Lu]Lu-Dar-PSMA-617 in PBS and BSA at 37°C

The Log *P* values of [^{177}Lu]Lu-Dar-PSMA-617 and [^{177}Lu]Lu-DOTA-PSMA-617 were -2.42 ± 0.04 and -3.12 ± 0.16, respectively.

Crystal structure analysis

The crystal structure of Ga-Dar complex reveals the coordination mode of a pair of Ga^{3+} cations in the 24-membered macrocyclic chelator Dar (as shown in Fig. 3a). The two gallium atoms are located within two cavities of the large macrocyclic ring as a single Ga-Dar complex, which demonstrates a symmetrical structure. Each gallium atom is six-coordinated to one phenolic hydroxyl oxygen, one pyridine nitrogen, two aliphatic nitrogen, and two carboxyl oxygen. Crystal data are given in Supplementary Tables 2–3. The coordination distance of Ga-O is in a range of 1.856–1.986 Å, in which the shortest distance is Ga-phenolic oxygen and the longest is Ga-carboxyl oxygen. The coordination distance of Ga-N is in a range of 2.008–2.104 Å, in which the pyridine nitrogen atom is closer to the metal ion Ga^{3+} than the aliphatic nitrogen atom.

The crystal structure of Lu-Dar complex reveals the coordination mode of a Lu^{3+} cation in the 24-membered macrocyclic chelator Dar (as shown in Fig. 3b). A lutetium atom is coordinated to two phenolic hydroxyl oxygen, one pyridine

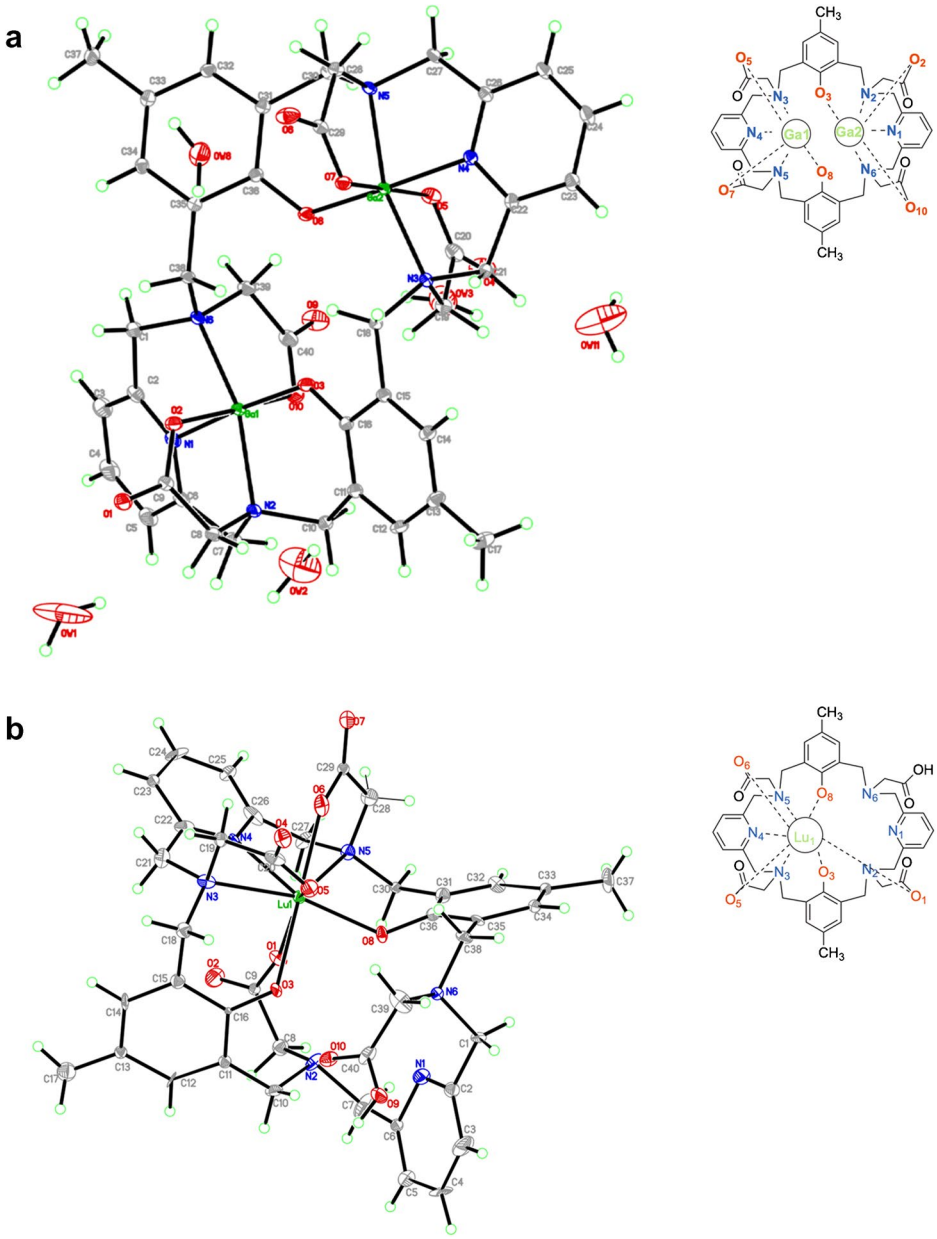

Fig. 3 Crystal structure of metal Dar complex. **a** Ga-Dar. **b** Lu-Dar

nitrogen, two aliphatic nitrogen, and three carboxyl oxygen, forming an eight-coordinated crystal structure. Crystal data are given in Supplementary Tables 4–5. The coordination distance of Lu-O is in a range of 2.139–2.453 Å and that of Lu-N is in a range of 2.462–2.539 Å.

Micro-PET imaging and pharmacokinetics studies of Dar-PSMA-617

[^{68}Ga]Ga-NOTA-PSMA-617, [^{68}Ga]Ga-DOTA-PSMA-617, and [^{68}Ga]Ga-Dar-PSMA-617 PET images demonstrated favorable tumor uptake and differentiate uptakes in other organs in vivo (as shown in Fig. 4a–b). The tumor uptake of [^{68}Ga]Ga-NOTA-PSMA-617, [^{68}Ga]Ga-DOTA-PSMA-617, and [^{68}Ga]Ga-Dar-PSMA-617 peaked with values of 8.48 ± 0.61%ID/g at 2 h p.i., 3.15 ± 1.22%ID/g at 25 min p.i., and 7.77 ± 1.15%ID/g at 4 h p.i., respectively. The tumor uptakes of [^{68}Ga]Ga-Dar-PSMA-617 from 2 to 6 h p.i. were almost twice than that of [^{68}Ga]Ga-DOTA-PSMA-617, showing that [^{68}Ga]Ga-Dar-PSMA-617 has a higher detection ability on tumor diagnosis imaging than that of [^{68}Ga]Ga-DOTA-PSMA-617, especially at later time points (Fig. 4c). The kidney uptakes were higher as shown on [^{68}Ga]Ga-Dar-PSMA-617 images than that on [^{68}Ga]Ga-DOTA-PSMA-617 PET images. The kidney uptake of [^{68}Ga]

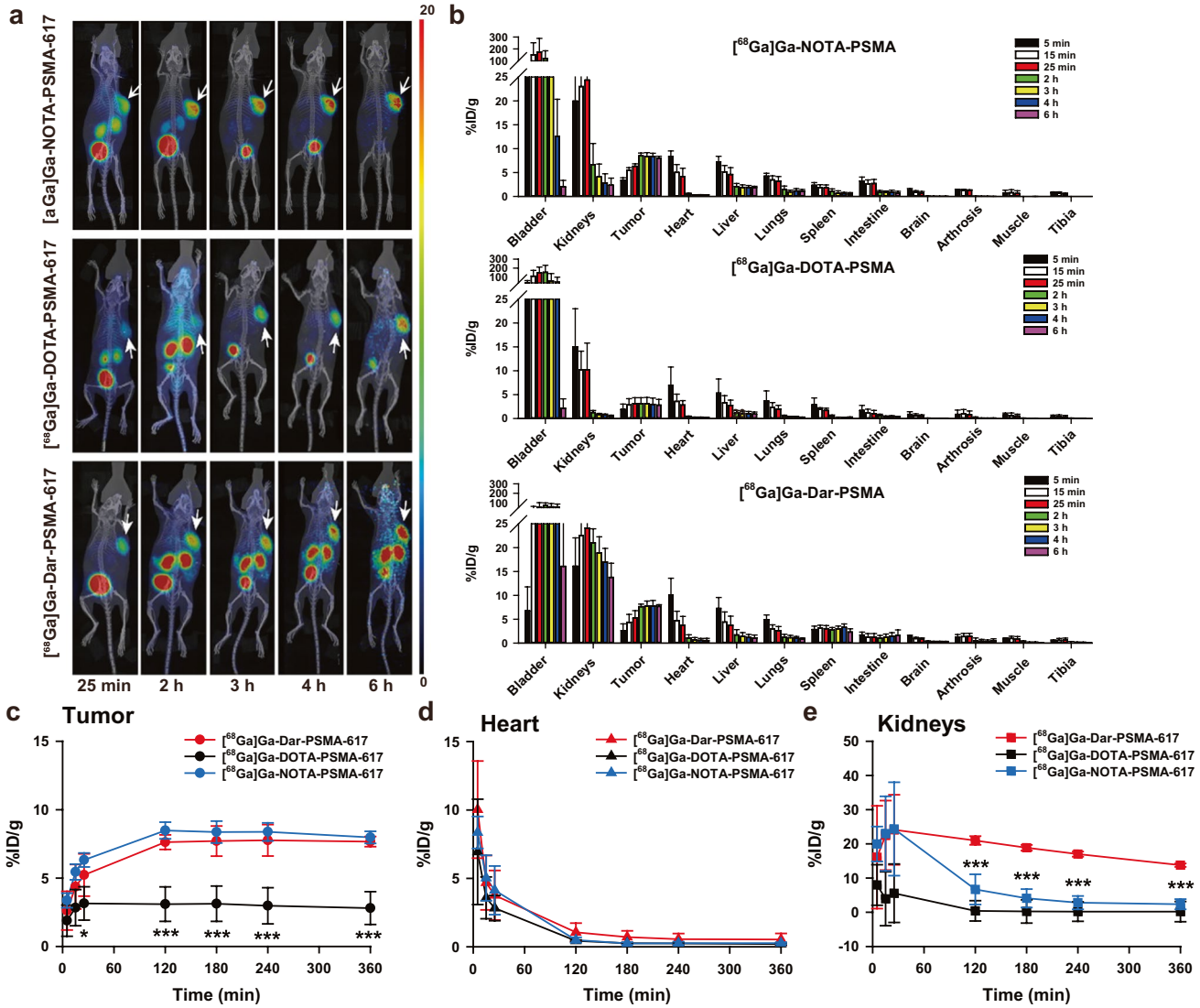

Fig. 4 Micro-PET imaging studies of [^{68}Ga]Ga-NOTA-PSMA-617, [^{68}Ga]Ga-DOTA-PSMA-617, and [^{68}Ga]Ga-Dar-PSMA-617 in LNCaP tumor-bearing nude mice. **a** and **b** Representative small-animal PET/CT fusion images and in vivo biodistribution of three tracers. **c**-**e** Time-activity curves of tumor, heart, and kidney uptake of three tracers. Data are presented as %ID/g ± SD (n = 4–5). *P < 0.05 and ***P < 0.001

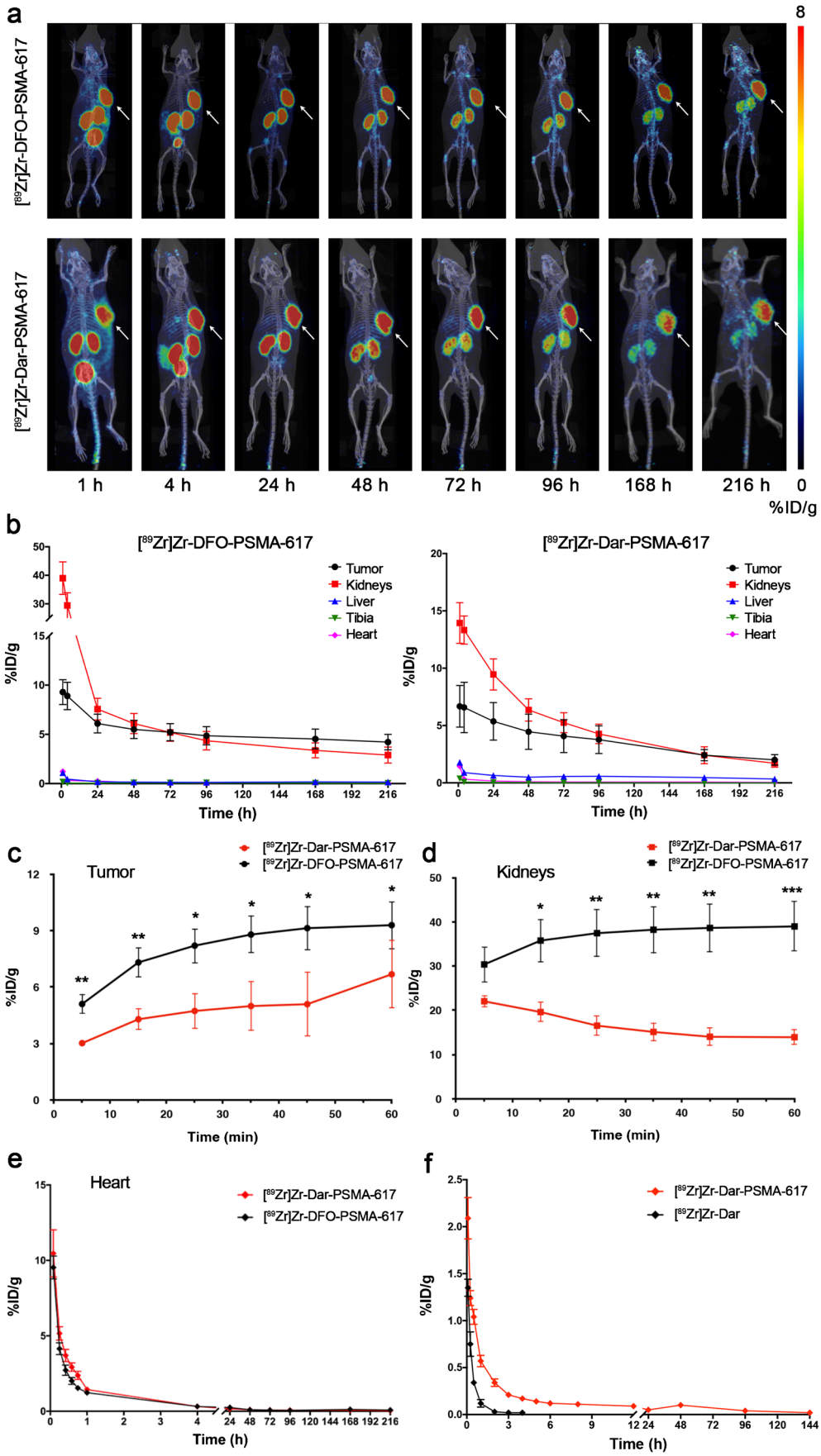
a
[89Zr]Zr-DFO-PSMA-617
[89Zr]Zr-Dar-PSMA-617
1 h
4 h
24 h
48 h
72 h
96 h
168 h
216 h
8
0
%ID/g
b
[89Zr]Zr-DFO-PSMA-617
[89Zr]Zr-Dar-PSMA-617
Tumor
Kidneys
Liver
Tibia
Heart
%ID/g
Time (h)
c
Tumor
[89Zr]Zr-Dar-PSMA-617
[89Zr]Zr-DFO-PSMA-617
%ID/g
Time (min)
d
Kidneys
[89Zr]Zr-Dar-PSMA-617
[89Zr]Zr-DFO-PSMA-617
%ID/g
Time (min)
e
Heart
[89Zr]Zr-Dar-PSMA-617
[89Zr]Zr-DFO-PSMA-617
%ID/g
Time (h)
f
[89Zr]Zr-Dar-PSMA-617
[89Zr]Zr-Dar
%ID/g
Time (h)

◂**Fig. 5** Micro-PET imaging and pharmacokinetics studies of [^{89}Zr]Zr-Dar-PSMA-617. **a** Representative small-animal PET/CT fusion images of [^{89}Zr]Zr-DFO-PSMA-617 and [^{89}Zr]Zr-Dar-PSMA-617 in LNCaP tumor-bearing nude mice. **b** Time-dependent uptake and retention of radioactivity in the main source organs after injection of [^{89}Zr]Zr-DFO-PSMA-617 and [^{89}Zr]Zr-Dar-PSMA-617 from 1 to 216 h in LNCaP tumor-bearing nude mice. **c** and **d** Time-activity curves of tumor and kidney uptake from 5 to 60 min in LNCaP tumor-bearing nude mice. **e** Time-activity curves of heart uptake from 5 min to 216 h in LNCaP tumor-bearing nude mice. Data are presented as %ID/g ± SD (n = 4–6). **f** Blood clearance of [^{89}Zr]Zr-Dar and [^{89}Zr]Zr-Dar-PSMA-617 after a single intravenous administration in male SD rats (n = 12). *P < 0.05 and **P < 0.01

Ga-Dar-PSMA-617 (24.10 ± 8.56%ID/g) was equivalent to that of [^{68}Ga]Ga-NOTA-PSMA-617 (24.36 ± 13.64%ID/g) at 25 min p.i., but [^{68}Ga]Ga-NOTA-PSMA-617 showed fast clearance in kidneys (Fig. 4e). There is little difference in the heart uptake of these three tracers (Fig. 4d).

PET images of [^{89}Zr]Zr-DFO-PSMA-617 and [^{89}Zr]Zr-Dar-PSMA-617 are depicted in Fig. 5a. The tumor uptakes of [^{89}Zr]Zr-DFO-PSMA-617 and [^{89}Zr]Zr-Dar-PSMA-617 both peaked at 1 h p.i., which were 9.29 ± 1.26%ID/g and 6.68 ± 1.82%ID/g, respectively (Fig. 5b and Fig. 5c). The tumor retention of [^{89}Zr]Zr-Dar-PSMA-617 from 4 to 216 h p.i. was from 6.58 ± 2.20 to 2.01 ± 0.46%ID/g, and that of [^{89}Zr]Zr-DFO-PSMA-617 was from 8.90 ± 1.39 to 4.21 ± 0.79%ID/g (Fig. 5b). The kidney uptake of [^{89}Zr]Zr-Dar-PSMA-617 was 13.94 ± 1.78%ID/g at 1 h p.i., which is half of [^{89}Zr]Zr-DFO-PSMA-617 (38.99 ± 5.70%ID/g). The blood half-life of [^{89}Zr]Zr-Dar-PSMA-617 was 1.27 h calculated by Fig. 5e. [^{89}Zr]Zr-Dar-PSMA-617 displayed rapid blood clearance over the 6-day time course, with 1.04 ± 0.08%ID/g at 0.5 h and 0.09 ± 0.02%ID/g at 12 h p.i.. The blood half-lives of [^{89}Zr]Zr-Dar and [^{89}Zr]Zr-Dar-PSMA-617 were 0.21 and 4.57 h, respectively (Fig. 5f).

Cell uptake, internalization, and efflux studies

[^{177}Lu]Lu-Dar-PSMA-617 showed much higher cell uptakes than that of [^{177}Lu]Lu-DOTA-PSMA-617 at 4 and 24 h of incubation. The high uptake in the LNCaP cells was nearly completely blocked by 2-PMPA for both radiolabeled peptides (Fig. 6a). Internalization studies of both radiolabeled peptides were followed of incubation at 4 h and 24 h. Within the first 4 h of incubation, [^{177}Lu]Lu-DOTA-PSMA-617 internalized a little faster than [^{177}Lu]Lu-Dar-PSMA-617, while [^{177}Lu]Lu-Dar-PSMA-617 showed increased internalization at 24 h and later (Fig. 6b). Furthermore, the efflux rates of [^{177}Lu]Lu-DOTA-PSMA-617 were similar to that of [^{177}Lu]Lu-DOTA-PSMA-617 (Fig. 6c).

Antitumor efficacy in vivo

To assess the therapeutic efficacy of [^{177}Lu]Lu-Dar-PSMA-617, different dosimetry was administered to randomized mice model. In vivo biodistribution experiments on LNCaP tumor-bearing mice were also performed along with the efficacy study. As shown in Fig. 7a, the SPECT imaging of [^{177}Lu]Lu-Dar-PSMA-617 exhibited more favorable tumor accumulation than that of [^{177}Lu]Lu-DOTA-PSMA-617. The tumor uptake of [^{177}Lu]Lu-Dar-PSMA-617 increased over time and exceeded 5%ID/g at each time point, while that of [^{177}Lu]Lu-DOTA-PSMA-617 only reached the peak of 3.56 ± 0.90%ID/g at 24 h p.i. (Fig. 7b). Interestingly, even the low-dose [^{177}Lu]Lu-Dar-PSMA-617 treatment group (9.25 MBq) showed slower tumor growth than that of both middle-dose and high-dose [^{177}Lu]Lu-DOTA-PSMA-617 treatment groups (18.5 MBq and 37 MBq) (Fig. 7c), indicating that the efficacy of [^{177}Lu]Lu-Dar-PSMA-617 at the low dose was remarkable. With the same middle dose (18.5 MBq), the tumor volumes of [^{177}Lu]Lu-Dar-PSMA-617 treatment group were less than 120 mm^3 from day 12 all the way to the end of study, which were well below that of the [^{177}Lu]Lu-DOTA-PSMA-617 treatment group which is over 500 mm^3. Furthermore, there was no significant difference in body weight among the treatment groups except the high-dose [^{177}Lu]Lu-Dar-PSMA-617 (37 MBq) (Supplementary Fig. 10). However, the survival period of the high-dose [^{177}Lu]Lu-Dar-PSMA-617 group (37 MBq) was significantly shorter, indicating that there were unknown side effects at the high dose of [^{177}Lu]Lu-Dar-PSMA-617 treatment. The area under curve (AUC) of tumor uptakes of [^{177}Lu]Lu-Dar-PSMA-617 and [^{177}Lu]Lu-DOTA-PSMA-617 is calculated and depicted in Fig. 7d, which is 645.5 and 330.2%ID/g·h, respectively. Collectively, [^{177}Lu]Lu-Dar-PSMA-617 provided better pharmacokinetics than that of [^{177}Lu]Lu-DOTA-PSMA-617 in xenograft models and might be clinically applied for cancer therapy at low-dose level.

Micro-PET imaging studies of Dar-KN035

Micro-PET imaging scans of MC38&MC38-hPD-L1 tumor-bearing mice were performed after i.v. administration of [^{89}Zr]Zr-DFO-KN035 (Fig. 8a) and [^{89}Zr]Zr-Dar-KN035 (Fig. 8c). [^{89}Zr]Zr-Dar-KN035 was mainly distributed in the liver and kidneys, followed by the heart, spleen, MC38-hPD-L1 tumor, lungs, MC38 tumor, bone, joint, and intestine, with low distribution in the muscle, tibia, and brain. The liver uptake of [^{89}Zr]Zr-Dar-KN035 was half of that of [^{89}Zr]Zr-DFO-KN035 and declined progressively. The liver uptake of [^{89}Zr]Zr-DFO-KN035 was over 20%ID/g during the

observed period (Fig. 8b), while that of [^{89}Zr]Zr-Dar-KN035 declined from 12.57 ± 1.07 to 7.42 ± 0.78%ID/g (Fig. 8d). [^{89}Zr]Zr-Dar-KN035 uptake in the tumor of MC38-hPD-L1 model was higher than that in MC38 model at each time point. The uptake of MC38-hPD-L1 tumor reached the peak at 24 h p.i. (5.82 ± 1.21%ID/g), and MC38 tumor uptake also peaked at 24 h p.i. (4.21 ± 0.48%ID/g) (Fig. 8d).

Ex vivo biodistribution studies

The ratios of kidneys-to-blood, liver-to-blood, tibia-to-blood, tumor-to-blood, tumor-to-muscle, and tumor-to-kidneys were calculated. The ex vivo biodistribution data of [^{89}Zr]Zr-Dar-PSMA-617 showed that the tumor uptake was the highest tissue except the kidneys. The calculation showed that the tumor-to-blood ratio of [^{89}Zr]Zr-Dar-PSMA-617 was 7.84 ± 0.39 and tumor-to-muscle ratio of [^{89}Zr]Zr-Dar-PSMA-617 was 68.48 ± 21.24 at 96 h p.i. The tumor-to-blood ratio of [^{89}Zr]Zr-DFO-PSMA-617 was 28.90 ± 13.16 and the tumor-to-muscle ratio of [^{89}Zr]Zr-DFO-PSMA-617 was 14.03 ± 0.01 at 96 h p.i..

The ex vivo biodistribution data of [^{177}Lu]Lu-DOTA-PSMA-617 and [^{177}Lu]Lu-Dar-PSMA-617 in LNCaP tumor-bearing nude mice at 72 h p.i. showed that the tumor uptakes were 3.85 ± 1.06%ID/g and 4.00 ± 4.52%ID/g, respectively. Since the uptake value of muscle and blood is close to the background, the deviation of tumor-to-muscle ratio and tumor-to-blood ratio is too large for reference only.

The ex vivo biodistribution data of [^{89}Zr]Zr-DFO-KN035 and [^{89}Zr]Zr-Dar-KN035 in MC38&MC38-hPD-L1 tumor-bearing nude mice at 168 h p.i. were obtained. [^{89}Zr]Zr-DFO-KN035 uptake in the tumor of MC38-hPD-L1 model was 3.13 ± 0.35%ID/g and that of MC38 model was 2.45 ± 0.03%ID/g. [^{89}Zr]Zr-Dar-KN035 uptake in the tumor of MC38-hPD-L1 model was 3.99 ± 0.62%ID/g and that of MC38 model was 3.48 ± 0.60%ID/g. The ex vivo biodistribution data are consistent with the in vivo ROI analysis.

Discussion

To our knowledge, there is lack of bifunctional chelator that can radiolabel with multiple types of radionuclides at ambient temperature. Here, we tried to construct a novel chelator to achieve the purpose for using the same precursor labeling multiple radionuclides without heating process. In this study, the capability of designed Dar to coordinate ^{68}Ga, ^{89}Zr, and ^{177}Lu was achieved in high radiolabeling yield at room temperature. From a coordination point of view, Dar contains phenolic oxygen, carboxyl oxygen, pyridine nitrogen, and aliphatic nitrogen which are able to act as donor atoms in metal complexes. Two phenolic oxygen atoms and two pyridyl nitrogen atoms orient toward the center of the macrocycle. The four amino nitrogen atoms covalently linked to four carboxyl oxygen lie on each corner of a square plane around the center of Dar coordinating to the positive charged metal ion. The selection of the appropriate both "hard and soft" combination of donor atoms with a relatively proper charge density and the geometry of the chelator itself impart complexes with more flexibility for different kinds of metal ions, mainly contributing to thermodynamic stability. In addition, the macrocyclic nature of Dar with high geometric and topological rigidity makes metal

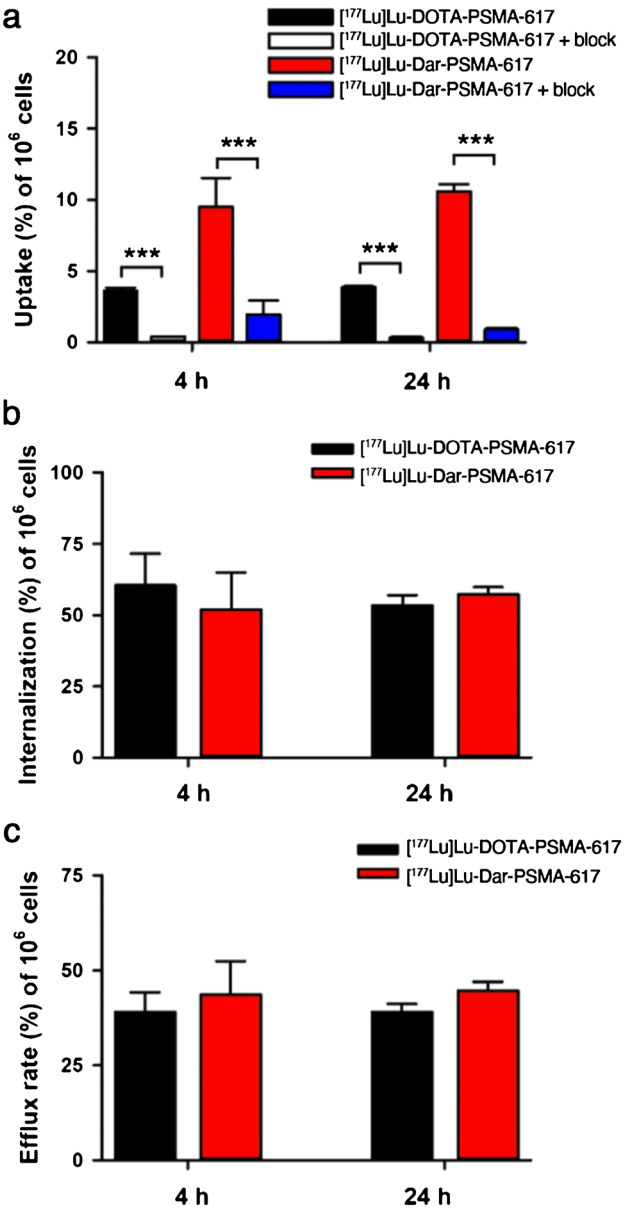

Fig. 6 Cell uptake (**a**), internalization (**b**), and efflux (**c**) studies of [^{177}Lu]Lu-Dar-PSMA-617 and [^{177}Lu]Lu-DOTA-PSMA-617 in LNCaP tumor cells. Data are presented as mean ± SD, ***$P < 0.001$

complexes kinetically inert in vivo. The unique property of Dar explains the mechanism of coordination between Dar and radionuclide with high stability, which is confirmed by in vitro stability study (Fig. 2) and the low uptake of tibia in vivo (Fig. 4, Fig. 5, and Fig. 7). The designed structure of Dar with enriched donors and flexible size can be expanded or twisted to allow more kinds of radiometal ions coordinating into the cavities inside Dar, including divalent, trivalent, and tetravalent radionuclides [28, 29, 32]. Therefore, Dar is proven capable on radiolabeling a variety of diagnostic and therapeutic radionuclides for precision theranostics of cancer.

PSMA-617 was chosen as a tool compound of small molecule targeting carrier for its well-validated in vitro and in vivo tumor targeting properties. Three most representative nuclides, $^{68}Ga^{3+}$, $^{89}Zr^{4+}$, and $^{177}Lu^{3+}$, were selected to radiolabel Dar-PSMA-617. Radiolabeled [^{68} Ga]Ga-Dar-PSMA-617 was used for PET diagnosis, [^{89}Zr]Zr-Dar-PSMA-617 was used for prolonged biodistribution study, and [^{177}Lu]Lu-Dar-PSMA-617 was used for tumor treatment efficacy evaluation. These three preclinical experiments provided a preliminary basis for later clinical exploration using the high quantitative PET imaging for prolonged monitoring, and optimizing therapeutic dosimetry in cancer patients.

It can be seen from Fig. 4c that the tumor uptake of [^{68}Ga]Ga-Dar-PSMA-617 peaked at 4 h p.i. with a value of 7.77 ± 1.15%ID/g. As a comparison, the tumor uptake of [^{68}Ga]Ga-NOTA-PSMA-617 peaked at 2 h p.i. with a value of 8.48 ± 0.61%ID/g and that of [^{68}Ga]Ga-DOTA-PSMA-617 peaked at 25 min p.i. with a value of 3.15 ± 1.22%ID/g. All three compounds showed good tumor uptake and retention ability in the period of 2–6 h p.i. Taken together, [^{68}Ga]Ga-Dar-PSMA-617 tumor uptake capacity is between [^{68}Ga]Ga-NOTA-PSMA-617 and [^{68}Ga]Ga-DOTA-PSMA-617, which means that different chelators can partially modulate the tumor uptake property and organs/tissue retention of the target molecule. With these results, we find that NOTA is still the best-fit chelator for $^{68}Ga^{3+}$ nuclide with a small radius (ion radius 62 pm) [9, 33]. Dar is a universal chelator with large cavity and multiple coordinating donors for

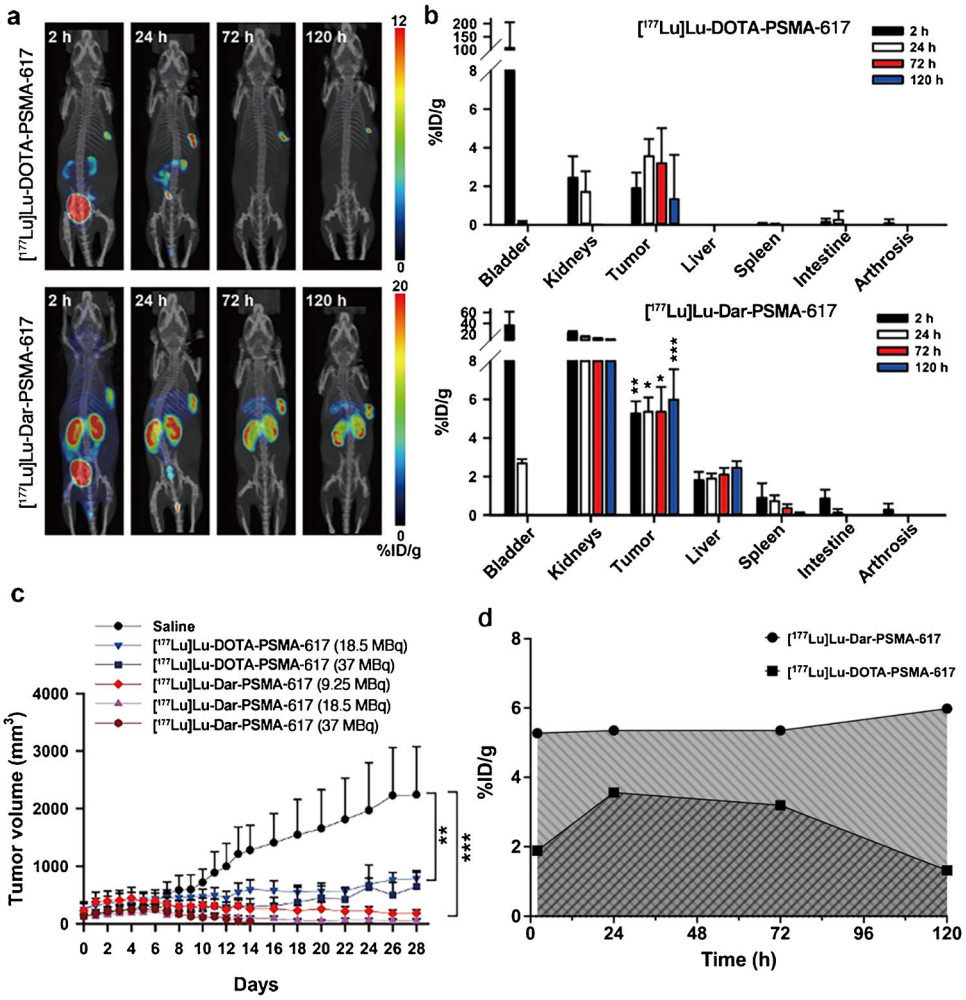

Fig. 7 Micro-SPECT imaging studies and therapeutic efficacy of [^{177}Lu]Lu-DOTA-PSMA-617 and [^{177}Lu]Lu-Dar-PSMA-617 in LNCaP tumor-bearing mice. **a** and **b** Representative small-animal SPECT/CT fusion images and in vivo biodistribution of [^{177}Lu]Lu-DOTA-PSMA-617 (37 MBq) and [^{177}Lu]Lu-Dar-PSMA-617 (37 MBq) ($n = 4$). **c** Mean volumes of LNCaP tumors in mice that received [^{177}Lu]Lu-Dar-PSMA-617 in comparison with [^{177}Lu]Lu-DOTA-PSMA-617 ($n = 7$–10). **d** Uptake accumulation curve of tumor uptake of [^{177}Lu]Lu-DOTA-PSMA-617 (37 MBq) and [^{177}Lu]Lu-Dar-PSMA-617 (37 MBq). Data are presented as the average value + SD. *$P < 0.05$, **$P < 0.01$, and ***$P < 0.001$

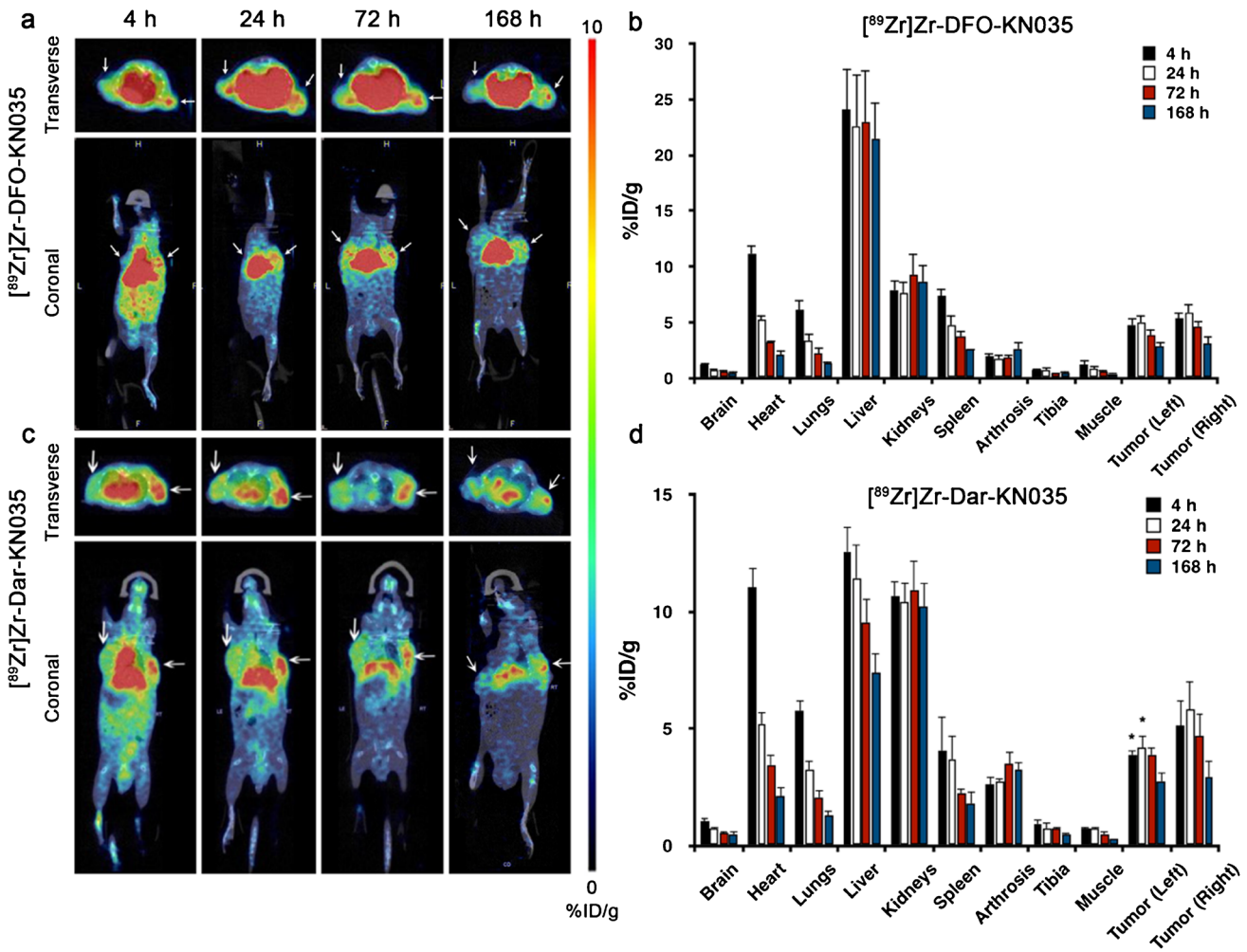

Fig. 8 Micro-PET imaging studies of [^{89}Zr]Zr-Dar-KN035 and [^{89}Zr]Zr-DFO-KN035 in MC38&MC38-hPD-L1 tumor-bearing nude mice (arrows on the left side, positions of MC38 tumors; arrows on the right side, positions of MC38-hPD-L1 tumors). **a** and **c** Representative small-animal PET images. **b** and **d** Time-dependent uptake and retention of radioactivity in the main source organs. Data are presented as %ID/g ± SD (n = 4). *P < 0.05

radiometals of large radius, but it is not a good option for $^{68}Ga^{3+}$ labeling.

On the other hand, [^{89}Zr]Zr-Dar-PSMA-617 achieved equivalent tumor uptake against that of [^{89}Zr]Zr-DFO-PSMA-617 as shown in Fig. 5, both peaked around 1 h p.i. and gradually declined over time, where the almost identical uptake values were observed between 24 and 216 h p.i. (3–5%ID/g). Meanwhile, the kidney uptake of [^{89}Zr]Zr-Dar-PSMA-617 showed a lower early phase uptake than that of [^{89}Zr]Zr-DFO-PSMA-617 within 24 h p.i.. The tibia uptakes of both tracers were low enough to indicate their good stability in vivo. The ex vivo biodistribution data of the two ^{89}Zr-labeled compounds (Table 1) are consistent with the in vivo ROI analysis. The results of in vivo and ex vivo experiments demonstrated that the Dar is a qualified alternative to DFO for radiolabeling with ^{89}Zr nuclide. This will waiver an additional chelator conjugation when researchers intend to use ^{89}Zr to have a prolonged observation with more sensitive and quantitative PET imaging study for conjugated biomolecule, or even small molecules such as PSMA-617.

Probably most advantage of the Dar demonstrated here is that when the chelator is used for labeling $^{177}Lu^{3+}$, the therapeutic lanthanide radionuclide with large ion radius (84.8 pm), the complex [^{177}Lu]Lu-Dar-PSMA-617 can be formed at room temperature. The in vitro uptake study demonstrated a higher tumor cell–associated proportion for [^{177}Lu]Lu-Dar-PSMA-617 (Fig. 6) but similar internalization and efflux rate, compared to the data from using [^{177}Lu]Lu-DOTA-PSMA-617 as control. The superior tumor uptake/retention for [^{177}Lu]Lu-Dar-PSMA-617 was extended to in vivo in mice-bearing LNCaP xenografts (Fig. 7a, 7b, and 7d). This superior tumor uptake/exposure led to a more efficacious inhibition on tumor growth (Fig. 7c). It has not escaped our notice that using Dar as chelator also resulted in

an elevated persistent radioactivity retention in the kidneys, liver, and other organs. The high tumor cell uptake both in vitro and in vivo may be attributed to the superior stability of Dar-mediated ^{177}Lu labeling, i.e., that more intact ^{177}Lu-labeled targeting molecule available for re-uptake, which also resulted in a more efficacious tumor growth inhibition.

Dar introduces bisphenol hydroxyl and bipyridine moieties to improve the lipophilicity of [^{177}Lu]Lu-Dar-PSMA-617, resulting in prolonging blood circulation time and improving tumor uptake and retention [34, 35]. This result is similar to the mechanism of [^{177}Lu]Lu-EB-PSMA-617 and [^{177}Lu]Lu-L14 [23, 36]. Sequentially, the kidney uptake of [^{177}Lu]Lu-Dar-PSMA-617 increased due to the introducing aromatic moieties in the chelator. The same result was observed on [^{177}Lu]Lu-EB-PSMA-617 that had a high radiation dose in the kidneys [36, 37]. However, the latest research shows that even in the treatment of mCRPC patients with chronic renal failure or renal dysfunction, no negative effects on renal function caused by PSMA-RLT were observed [38]. In our efficacy study, the body weight of testing mice had not been changed significantly for [^{177}Lu]Lu-Dar-PSMA-617 treatment, indicating a controllable renal toxicity in mouse tumor model.

The success of Dar's ability radiolabeling metals at room temperature was also extended to radiolabel the temperature-sensitive biologics. The results in which we used a nanobody as a tool biologic molecule are convincing for using Dar as a universal chelator for radiolabeling both small molecule/peptide and large biologic molecule that may not tolerate heating process required by commonly used cyclic chelators such as DOTA and NOTA. Dar was also designed to have potential as a universal bifunctional chelator for radiolabeling various radiometals (at least ^{68}Ga, ^{177}Lu, and ^{89}Zr tested) commonly used for clinical imaging and therapy, especially for labeling radiometals with large radius, such as $^{89}Zr^{4+}$ (80 pm) and $^{177}Lu^{3+}$ (84.8 pm).

The last but not the least, there still are several imperfect aspects of this novel chelator needing to be investigated for future improvement. Those include the potential tendency of having two small metal nuclides into the same chelator cavity and the possible high uptake/retention in normal organs/tissue, especially in the kidneys. Based on current experiment results, NOTA for $^{68}Ga^{3+}$ and DOTA for $^{177}Lu^{3+}$ are still the golden-standard chelators for peptide receptor radionuclide therapy (PRRT).

Table 1 biodistribution data in the unit of %ID/g ± SD

Organs and tissues	[^{89}Zr]Zr-DFO-PSMA-617	[^{89}Zr]Zr-Dar-PSMA-617	[^{177}Lu]Lu-DOTA-PSMA-617	[^{177}Lu]Lu-Dar-PSMA-617	[^{89}Zr]Zr-DFO-KN035	[^{89}Zr]Zr-Dar-KN035
	96 h	96 h	72 h	72 h	168 h	168 h
Kidneys	6.63 ± 1.93	7.59 ± 1.50	0.29 ± 0.11	8.37 ± 2.67	12.25 ± 10.35	25.62 ± 8.31
Spleen	0.01 ± 0.01	1.00 ± 0.12	0.05 ± 0.01	1.62 ± 0.41	4.25 ± 1.04	3.66 ± 0.40
Tibia	1.22 ± 0.51	0.85 ± 0.38	0.03 ± 0.01	0.49 ± 0.12	2.58 ± 0.96	4.86 ± 0.52
Liver	0.19 ± 0.02	0.68 ± 0.07	0.03 ± 0.01	1.67 ± 0.11	19.8 ± 2.07	7.91 ± 1.11
Arthrosis	1.49 ± 0.67	0.58 ± 0.06	0.03 ± 0.01	0.65 ± 0.12	2.99 ± 1.11	5.58 ± 1.63
Heart	0.01 ± 0.01	0.39 ± 0.21	0.02 ± 0.01	0.18 ± 0.06	3.56 ± 0.67	1.92 ± 0.34
Lungs	0.36 ± 0.05	0.21 ± 0.06	0.02 ± 0.01	0.30 ± 0.04	2.50 ± 0.04	2.47 ± 0.48
Pancreas	0.01 ± 0.01	0.20 ± 0.05	0.01 ± 0.01	0.10 ± 0.03	3.40 ± 0.80	2.14 ± 0.81
Stomach	0.01 ± 0.01	0.16 ± 0.03	0.01 ± 0.01	0.16 ± 0.04	1.12 ± 0.56	1.21 ± 0.23
Large intestine	0.10 ± 0.01	0.13 ± 0.05	0.01 ± 0.01	0.15 ± 0.02	1.03 ± 0.03	0.74 ± 0.05
Brain	0.01 ± 0.01	0.10 ± 0.06	0.01 ± 0.01	0.02 ± 0.01	0.23 ± 0.05	0.20 ± 0.05
Small intestine	0.07 ± 0.04	0.07 ± 0.01	0.01 ± 0.01	0.10 ± 0.02	0.84 ± 0.14	0.60 ± 0.09
Blood	0.27 ± 0.08	0.77 ± 0.14	0.01 ± 0.01	0.04 ± 0.01	2.21 ± 0.14	2.36 ± 0.18
Muscle	0.46 ± 0.05	0.10 ± 0.01	0.01 ± 0.01	0.04 ± 0.01	0.65 ± 0.22	0.69 ± 0.26
Tumor (Left)	/	/	/	/	2.45 ± 0.03	3.48 ± 0.60
Tumor (Right)	8.77 ± 2.58	6.10 ± 1.34	3.85 ± 1.06	4.00 ± 4.52	3.13 ± 0.35	3.99 ± 0.62
Kidneys/Blood	24 73 ± 15.99	9.85 ± 1.53	34.3 ± 22.7	226.18 ± 45.35	5.45 ± 4.49	10.12 ± 4.32
Liver/Blood	0.76 ± 0.22	0.88 ± 0.09	2.89 ± 1.33	47.23 ± 13.24	8.98 ± 0.83	3.10 ± 0.52
Tibia/Blood	4.92 ± 4.02	1.06 ± 0.30	2.87 ± 1.48	14.32 ± 7.51	1.16 ± 0.36	2.09 ± 0.12
Tumor/Blood	28.90 ± 13.16	7.84 ± 0.39	433.23 ± 260.77	93.62 ± 83.18	1.43 ± 0.23	1.66 ± 0.23
Tumor/Muscle	14.03 ± 0.01	68.48 ± 21.24	385.17 ± 105.57	108.2 ± 120.21	5.14 ± 1.57	5.71 ± 2.11
Tumor/Kidneys	1.34 ± 0.25	0.81 ± 0.11	13.66 ± 2.37	0.40 ± 0.35	1.65 ± 2.57	0.19 ± 0.08

Conclusion

A novel macrocyclic ligand Dar and its Dar-PSMA-617 conjugate were successfully synthesized and fully characterized by NMR spectra and crystallography. The in vitro and in vivo data demonstrated that Dar has potential to constitute a useful platform in radiopharmaceutical research and application on radiometal-labeling targeted molecules under physiological condition for theranostics of cancer.

Supplementary Information The online version contains supplementary material available at https://doi.org/10.1007/s00259-022-05750-8.

Acknowledgements The authors wish to acknowledge the National Natural Science Foundation of China and China Postdoctoral Science Foundation for the support of this work.

Author contribution XBT and ZW conceived the idea of the project. JFX wrote the manuscript in addition to designing, performing, and analyzing all experiments. JFX, FC, and WBF performed the experiments. JD, JJC, and SHL collected the information on animals. SHL and CRG assisted with data analysis. ZGL, CRG, QHZ, ZW, and XBT designed, supervised, and analyzed all experiments, in addition to assisting with manuscript preparation. All authors read and approved the final manuscript.

Funding This work was financially supported by the National Natural Science Foundation of China projects (Grant No. 11975123) and China Postdoctoral Science Foundation (Grant No. 2021T140321).

Data availability Not applicable.

Declarations

Ethics approval All animal studies were performed in accordance with the protocols provided in the Guide for the Care and Use of Medical Laboratory Animals (Ministry of Health, China).

Consent to participate Not applicable.

Consent for publication Not applicable.

Conflict of interest The authors declare no competing interests.

References

1. Synowiecki MA, Perk LR, Nijsen JFW. Production of novel diagnostic radionuclides in small medical cyclotrons. EJNMMI Radiopharm Chem. 2018;3:3. https://doi.org/10.1186/s41181-018-0038-z.
2. Radchenko V, Morgenstern A, Jalilian AR, Ramogida CF, Cutler C, Duchemin C, et al. Production and supply of alpha-particle-emitting radionuclides for targeted alpha-therapy. J Nucl Med. 2021;62:1495–503. https://doi.org/10.2967/jnumed.120.261016.
3. Talip Z, Favaretto C, Geistlich S, Meulen NPV. A step-by-step guide for the novel radiometal production for medical applications: case studies with 68Ga, 44Sc, 177Lu and 161Tb. Molecules. 2020;25:966. https://doi.org/10.3390/molecules25040966.
4. do Carmo SJC, Scott PJH, Alves F. Production of radiometals in liquid targets. EJNMMI Radiopharm Chem. 2020;5:2. https://doi.org/10.1186/s41181-019-0088-x.
5. Zhou X, Dong L, Shen L. Hydroxypyridinones as a very promising platform for targeted diagnostic and therapeutic radiopharmaceuticals. Molecules. 2021;26. https://doi.org/10.3390/molecules26226997.
6. Witney TH, Blower PJ. The chemical tool-kit for molecular imaging with radionuclides in the age of targeted and immune therapy. Cancer Imaging. 2021;21:18. https://doi.org/10.1186/s40644-021-00385-8.
7. Guleria M, Das T, Amirdhanayagam J, Sarma HD, Dash A. Comparative evaluation of using NOTA and DOTA derivatives as bifunctional chelating agents in the preparation of 68Ga-labeled porphyrin: impact on pharmacokinetics and tumor uptake in a mouse model. Cancer Biother Radiopharm. 2018;33:8–16. https://doi.org/10.1089/cbr.2017.2337.
8. Kelly JM, Amor-Coarasa A, Nikolopoulou A, Kim D, Williams C Jr, Vallabhajosula S, et al. Assessment of PSMA targeting ligands bearing novel chelates with application to theranostics: stability and complexation kinetics of 68Ga3+, 111In3+, 177Lu3+ and 225Ac3+. Nucl Med Biol. 2017;55:38–46. https://doi.org/10.1016/j.nucmedbio.2017.10.001.
9. Okoye NC, Baumeister JE, Khosroshahi FN, Hennkens HM, Jurisson SS. Chelators and metal complex stability for radiopharmaceutical applications. Radiochim Acta. 2019;107:1087–120. https://doi.org/10.1515/ract-2018-3090.
10. Price EW, Orvig C. Matching chelators to radiometals for radiopharmaceuticals. Chem Soc Rev. 2014;43:260–90. https://doi.org/10.1039/c3cs60304k.
11. Tsionou MI, Knapp CE, Foley CA, Munteanu CR, Cakebread A, Imberti C, et al. Comparison of macrocyclic and acyclic chelators for gallium-68 radiolabelling. RSC Adv. 2017;7:49586–99. https://doi.org/10.1039/c7ra09076e.
12. Holland JP, Divilov V, Bander NH, Smith-Jones PM, Larson SM, Lewis JS. 89Zr-DFO-J591 for immunoPET of prostate-specific membrane antigen expression in vivo. J Nucl Med. 2010;51:1293–300. https://doi.org/10.2967/jnumed.110.076174.
13. Fischer G, Seibold U, Schirrmacher R, Wangler B, Wangler C. 89Zr, a radiometal nuclide with high potential for molecular imaging with PET: chemistry, applications and remaining challenges. Molecules. 2013;18:6469–90. https://doi.org/10.3390/molecules18066469.
14. Sneddon D, Cornelissen B. Emerging chelators for nuclear imaging. Curr Opin Chem Biol. 2021;63:152–62. https://doi.org/10.1016/j.cbpa.2021.03.001.
15. Pandya DN, Bhatt N, An GI, Ha YS, Soni N, Lee H, et al. Propylene cross-bridged macrocyclic bifunctional chelator: a new design for facile bioconjugation and robust 64Cu complex stability. J Med Chem. 2014;57:7234–43. https://doi.org/10.1021/jm500348z.
16. Zhai C, Summer D, Rangger C, Franssen GM, Laverman P, Haas H, et al. Novel bifunctional cyclic chelator for (89)Zr labeling-radiolabeling and targeting properties of RGD conjugates. Mol Pharm. 2015;12:2142–50. https://doi.org/10.1021/acs.molpharmaceut.5b00128.
17. Heskamp S, Raave R, Boerman O, Rijpkema M, Goncalves V, Denat F. (89)Zr-immuno-positron emission tomography in oncology: state-of-the-art (89)Zr radiochemistry. Bioconjug Chem. 2017;28:2211–23. https://doi.org/10.1021/acs.bioconjchem.7b00325.
18. Deri MA, Ponnala S, Kozlowski P, Burton-Pye BP, Cicek HT, Hu C, et al. p-SCN-Bn-HOPO: a superior bifunctional chelator for (89)Zr immunoPET. Bioconjug Chem. 2015;26:2579–91. https://doi.org/10.1021/acs.bioconjchem.5b00572.
19. Baranyai Z, Tircsó G, Rösch F. The use of the macrocyclic chelator DOTA in radiochemical separations. Eur J Inorg Chem. 2019;2020:36–56. https://doi.org/10.1002/ejic.201900706.

20. Mewis RE, Archibald SJ. Biomedical applications of macrocyclic ligand complexes. Coord Chem Rev. 2010;254:1686–712. https://doi.org/10.1016/j.ccr.2010.02.025.
21. Virgolini I, Ambrosini V, Bomanji JB, Baum RP, Fanti S, Gabriel M, et al. Procedure guidelines for PET/CT tumour imaging with 68Ga-DOTA-conjugated peptides: 68Ga-DOTA-TOC, 68Ga-DOTA-NOC, 68Ga-DOTA-TATE. Eur J Nucl Med Mol Imaging. 2010;37:2004–10. https://doi.org/10.1007/s00259-010-1512-3.
22. Shi J, Liu Z, Jia B, Yu Z, Zhao H, Wang F. Potential therapeutic radiotracers: preparation, biodistribution and metabolic characteristics of 177Lu-labeled cyclic RGDfK dimer. Amino Acids. 2010;39:111–20. https://doi.org/10.1007/s00726-009-0382-0.
23. Banerjee SR, Kumar V, Lisok A, Chen J, Minn I, Brummet M, et al. 177Lu-labeled low-molecular-weight agents for PSMA-targeted radiopharmaceutical therapy. Eur J Nucl Med Mol Imaging. 2019;46:2545–57. https://doi.org/10.1007/s00259-019-04434-0.
24. Kang CS, Sun X, Jia F, Song HA, Chen Y, Lewis M, et al. Synthesis and preclinical evaluation of bifunctional ligands for improved chelation chemistry of 90Y and 177Lu for targeted radioimmunotherapy. Bioconjug Chem. 2012;23:1775–82. https://doi.org/10.1021/bc200696b.
25. Ruigrok EAM, van Vliet N, Dalm SU, de Blois E, van Gent DC, Haeck J, et al. Extensive preclinical evaluation of lutetium-177-labeled PSMA-specific tracers for prostate cancer radionuclide therapy. Eur J Nucl Med Mol Imaging. 2021;48:1339–50. https://doi.org/10.1007/s00259-020-05057-6.
26. Zeglis BM, Houghton JL, Evans MJ, Viola-Villegas N, Lewis JS. Underscoring the influence of inorganic chemistry on nuclear imaging with radiometals. Inorg Chem. 2014;53:1880–99. https://doi.org/10.1021/ic401607z.
27. Pandya DN, Bhatt N, Yuan H, Day CS, Ehrmann BM, Wright M, et al. Zirconium tetraazamacrocycle complexes display extraordinary stability and provide a new strategy for zirconium-89-based radiopharmaceutical development. Chem Sci. 2017;8:2309–14. https://doi.org/10.1039/c6sc04128k.
28. Wang Z, Reibenspies J, Martell AE. Design, synthesis, and X-ray structural characterization of new dinucleating macrocyclic ligands and a novel phenolate-bridged dilanthanum(III) complex. Inorg Chem. 1997;36:629–36. https://doi.org/10.1021/ic960665v.
29. Wang Z, Martell AE, Motekaitis RJ, Reibenspies J. The first systematic stability study of mononuclear and dinuclear iron(II) and iron(III) complexes incorporating a dinucleating macrocyclic ligand in aqueous solution†. J Chem Soci, Dalton Transactions. 1999:2441–50. https://doi.org/10.1039/a808051h.
30. Zhang F, Wei H, Wang X, Bai Y, Wang P, Wu J, et al. Structural basis of a novel PD-L1 nanobody for immune checkpoint blockade. Cell Discov. 2017;3:17004. https://doi.org/10.1038/celldisc.2017.4.
31. Benesova M, Schafer M, Bauder-Wust U, Afshar-Oromieh A, Kratochwil C, Mier W, et al. Preclinical evaluation of a tailor-made DOTA-conjugated PSMA inhibitor with optimized linker moiety for imaging and endoradiotherapy of prostate cancer. J Nucl Med. 2015;56:914–20. https://doi.org/10.2967/jnumed.114.147413.
32. Jurek PE, Jurek AM, Martell AE. Phosphate diester hydrolysis by mono- and dinuclear lanthanum complexes with an unusual third-order dependence. Inorg Chem. 2000;39:1016–20. https://doi.org/10.1021/ic9906961.
33. Wilson JJ, Ferrier M, Radchenko V, Maassen JR, Engle JW, Batista ER, et al. Evaluation of nitrogen-rich macrocyclic ligands for the chelation of therapeutic bismuth radioisotopes. Nucl Med Biol. 2015;42:428–38. https://doi.org/10.1016/j.nucmedbio.2014.12.007.
34. Vaughn BA, Ahn SH, Aluicio-Sarduy E, Devaraj J, Olson AP, Engle J, et al. Chelation with a twist: a bifunctional chelator to enable room temperature radiolabeling and targeted PET imaging with scandium-44. Chem Sci. 2020;11:333–42. https://doi.org/10.1039/c9sc04655k.
35. Joshi T, Graham B, Spiccia L. Macrocyclic metal complexes for metalloenzyme mimicry and sensor development. Acc Chem Res. 2015;48:2366–79. https://doi.org/10.1021/acs.accounts.5b00142.
36. Wang Z, Tian R, Niu G, Ma Y, Lang L, Szajek LP, et al. Single low-dose injection of Evans blue modified PSMA-617 radioligand therapy eliminates prostate-specific membrane antigen positive tumors. Bioconjug Chem. 2018;29:3213–21. https://doi.org/10.1021/acs.bioconjchem.8b00556.
37. Zang J, Fan X, Wang H, Liu Q, Wang J, Li H, et al. First-in-human study of (177)Lu-EB-PSMA-617 in patients with metastatic castration-resistant prostate cancer. Eur J Nucl Med Mol Imaging. 2019;46:148–58. https://doi.org/10.1007/s00259-018-4096-y.
38. Rosar F, Kochems N, Bartholoma M, Maus S, Stemler T, Linxweiler J, et al. Renal safety of [177Lu]Lu-PSMA-617 radioligand therapy in patients with compromised baseline kidney function. Cancers (Basel). 2021;13. https://doi.org/10.3390/cancers13123095.

Authors and Affiliations

Jianfeng Xu[1,2] · Fei Cai[1,2] · Zhigang Luo[2] · Wenbin Fan[2] · Juan Dai[2] · Jingjing Cui[2] · Shihong Li[2] · Changran Geng[1] · Qihuang Zheng[3] · Zheng Wang[2] · Xiaobin Tang[1]

✉ Zheng Wang
wangzheng@amschina.com

✉ Xiaobin Tang
tangxiaobin@nuaa.edu.cn

[1] Department of Nuclear Science and Technology, Nanjing University of Aeronautics and Astronautics, No. 29 Jiangjun Ave, Nanjing 211016, People's Republic of China

[2] JYAMS PET Research and Development Limited, No. 568 Longmian Ave, Nanjing 211100, People's Republic of China

[3] Department of Radiology and Imaging Sciences, Indiana University School of Medicine, 1345 West 16th Street, Room 112, Indianapolis, IN 46202, USA